Perseus arm – a new perspective on star formation and spiral structure in our home galaxy

M. Wienen,[1]★ C. M. Brunt,[1]★ C. L. Dobbs[1] and D. Colombo[2]

[1]*University of Exeter, School of Physics, Astrophysics Group, Stocker Road, Exeter EX4 4QL, UK*
[2]*Max-Planck-Institut für Radioastronomie, Auf dem Hügel 69, D-53121 Bonn, Germany*

ABSTRACT

Expansion of (sub)millimetre capabilities to high angular resolution offered with interferometers allows to resolve giant molecular clouds (GMCs) in nearby galaxies. This enables us to place the Milky Way in the context of other galaxies to advance our understanding of star formation in our own Galaxy. We, thus, remap ^{12}CO (1–0) data along the Perseus spiral arm in the outer Milky Way to a fixed physical resolution and present the first spiral arm data cube at a common distance as it would be seen by an observer outside the Milky Way. To achieve this goal, we calibrated the longitude–velocity structure of ^{12}CO gas of the outer Perseus arm based on trigonometric distances and maser velocities provided by the BeSSeL survey. The molecular gas data were convolved to the same spatial resolution along the whole spiral arm and regridded on to a linear scale map with the coordinate system transformed to the spiral arm reference frame. We determined the width of the Perseus spiral arm to be 7.8 ± 0.2 km s^{-1} around the kinematic arm centre. To study the large-scale structure, we derived the ^{12}CO gas mass surface density distribution of velocities, shifted to the kinematic arm centre, and arm length. This yields a variation of the gas mass surface density along the arm length and a compression of molecular gas mass at linear scale. We determined a thickness of ∼63 pc on average for the Perseus spiral arm and a centroid of the molecular layer of 8.7 pc.

Key words: surveys – stars: formation – ISM: clouds – ISM: molecules – Galaxy: structure – radio lines: ISM.

1 INTRODUCTION

The densest regions of giant molecular clouds (GMCs) are the birth-places of stars. The processes that drive GMC formation, evolution, and the star formation that eventually disperses them, are thought to occur primarily in spiral arms, and can be probed by panoramic mapping of spectral line emission from trace molecules in the clouds at millimetre wavelengths (Solomon & Rivolo 1989; Roman-Duval et al. 2010; García et al. 2014; Pan & Kuno 2017; Tosaki et al. 2017). The spatial distribution of GMCs is highly complex: they are fluid condensations within a more widely distributed atomic medium, they are highly fragmented, and often appear in large GMC complexes. In the efforts to understand our own Galaxy's star formation, the broader perspective offered by nearby galaxies with different global spiral structure, is very valuable. Two major problems prevent a clear path to quantitatively setting the Milky Way within the context provided by other galaxies: (1) spatial resolutions achievable in other galaxies are much poorer (by 1–2 orders of magnitude) than those achievable within our own Galaxy; cf. the spatial resolution of e.g. 1 pc at a distance of 5 kpc to GMCs from the Galactic Ring survey (Roman-Duval et al. 2010) versus 48 pc at a distance of 840 kpc to M33 (Gratier et al. 2010) or 98 pc at a distance of 14.4 Mpc to NGC 1068 (Tosaki et al. 2017) and (2) our Galaxy is observed from within, meaning that we do not have the privileged, clean, perspective of an external observer.

Comparison of Galactic and extragalactic studies is challenging, because one might typically be comparing small, resolved substructures in the Milky Way's GMCs to entire GMC complexes that are unresolved by observations in even the most nearby galaxies. Molecular clouds in our and other galaxies are primarily traced by spectral line emission from carbon monoxide molecules, mainly in the lowest (1–0) rotational transition that can be excited at the low (∼ 10 K) temperatures typical of the clouds. As a spectral line, it encodes position in 2D, Galactic longitude and latitude, and also line-of-sight velocity through the Doppler shift of the line. Detailed CO (1–0) maps of the central 9 kpc of M51 were observed by the Plateau de Bure Interferometer (PdBI) Arcsecond Whirlpool Survey (PAWS; Meidt et al. 2013; Pety et al. 2013; Schinnerer et al. 2013). These observations at a high resolution of 40 pc enable currently the identification of GMCs in external galaxies (Rosolowsky & Blitz 2005; Gratier et al. 2010, 2012; Donovan Meyer et al. 2013; Colombo et al. 2014; Leroy et al. 2015; Freeman et al. 2017; Colombo et al. 2019). Recent studies have investigated the physical state of GMCs (Hughes et al. 2013; Chen et al. 2016) and the spiral arm structure in the central part of nearby galaxies (Helfer et al. 2003; Schinnerer et al. 2013). High-resolution Galactic plane surveys enabled us to infer the spiral structure of the Milky Way and lead to efforts to model the Galactic structure (Dame, Hartmann & Thaddeus 2001; Roman-Duval et al. 2009; Reid et al. 2014; Vallée 2014; Pettitt, Ragan & Smith 2020). However, the most recent determination of Milky Way spiral structure kinematically determined from GMCs (fig. 16 in Rice et al. 2016; Miville-Deschênes, Murray & Lee 2017) is clearly a poorer view than that of NGC 628 (fig. 1 in Muraoka

★ E-mail: M.Wienen@exeter.ac.uk (MW); C.M.Brunt@exeter.ac.uk (CMB)
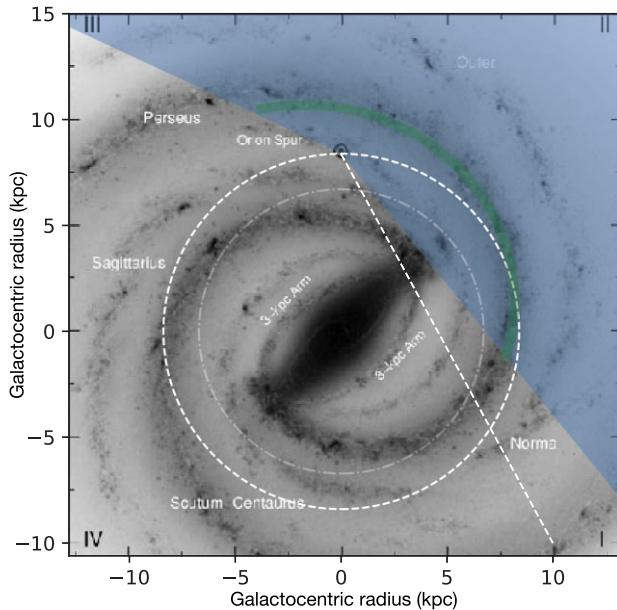
Figure 1. An artist conception of our Galaxy as it would appear from the perspective at the Northern Galactic Pole (NASA/JPL-Caltech/R. Hurt (SSC/Caltech)) is shown in the background. It gives an overview of the longitude range studied in this article that is indicated in blue shading with the Perseus arm illustrated as green shading. Emission from different spiral arms are contributing along the same line of sight in the inner Galaxy, which is indicated as white straight dashed line at a Galactic longitude of 30°. The solar circle and a smaller circular orbit are illustrated in dashed white, sources within that are influenced by the kinematic distance ambiguity.

et al. 2016) despite or in fact because of the Milky Way's immediate proximity. A clean separation of Galactic spiral arms is difficult.

To obtain a statistically significant sample of external galaxies within a reasonable observing time, the maximum achievable resolution from 20 to 40 pc is large compared to measurements in the Milky Way and prevents a detailed study of physical properties of substructures within GMCs. The analysis becomes more difficult when questioning whether the GMCs are gravitationally bound or not, and what the spectrum of GMC masses is. A comparison of galactic and extragalactic observations requires that we are sensitive to the same size and mass scales in both the Milky Way and external galaxies. Normally, the ideal solution to this problem would be to improve the spatial resolution of observations of distant galaxies so that they are comparable to those achievable in Milky Way surveys. But the necessary advances in instrumentation which will enable the mapping of a statistically notable number of complete galaxies will not happen in the foreseeable future. We therefore ask a different question: how would our high-resolution Milky Way GMCs appear to us if observed at extragalactic distances? The aims of our outer Perseus arm project are (i) to provide a direct comparison between the Milky Way and other galaxies at the same resolution, (ii) to investigate what distribution of GMC properties such as sizes, masses, velocity dispersions, luminosities would we derive, and (iii) to understand how degradation of resolution affects the comparison.

Distances to GMCs in the Milky Way are usually derived kinematically in the absence of direct distance measurements (Watson et al. 2003; Sewilo et al. 2004; Busfield et al. 2006; Anderson & Bania 2009; Roman-Duval et al. 2009; García et al. 2014; Wienen et al. 2015). The line-of-sight velocity can be used to predict distance, given a model of how the Galaxy rotates. In the inner parts of our

Galaxy (within the solar circle), this method is ambiguous, as two distances are geometrically possible for any observed velocity (see Fig. 1). In the outer Galaxy, the distance is unique and well-defined velocity structures of the spiral arms enable a clearer separation of those than in the inner Galaxy. Furthermore, molecular cloud complexes can be unambiguously identified and their formation and evolution can be studied in an environment, that is very different from the inner Galaxy, associated with a lower H I density (Heyer, Carpenter & Snell 2001; Heyer & Dame 2015), lower metallicity (Rudolph et al. 1997), lower cosmic ray flux (Bloemen et al. 1984) and higher gas-to-dust ratio (Giannetti et al. 2017).

This project is based on ^{12}CO (1–0) line data from the Exeter-FCRAO (Five College Radio Astronomy Observatory) survey (Brunt et al., in preparation) in the part of the Perseus arm in the outer Galaxy (see Fig. 1). The ^{12}CO line was observed at an order-of-magnitude improvement in angular resolution relative to the Galaxy-wide comprehensive survey with a resolution of 0°.125 by Dame et al. (2001). The data resolution is high enough to comfortably resolve GMCs along the spiral arm, with sufficient dynamic range to allow exploration of resolution issues that confound extragalactic studies. Furthermore, recently determined direct distances to high-mass star-forming sources in GMCs from the BeSSeL survey (Reid et al. 2014, 2016) can now enable accurate GMC distance and velocity calibration, using high-resolution observations of intense maser emission to deduce trigonometric parallaxes and line-of-sight velocities. We combined those with the highest angular resolution ^{12}CO observations available in the outer Galaxy and present the first distance-calibrated map of the Perseus spiral arm in the Outer Galaxy from the perspective of an observer outside the Milky Way. This article describes the preparation of the ^{12}CO data cube. Based on the released cube, a detailed study of the Perseus arm at fixed spatial resolution will follow.

Section 2 presents the observations of the ^{12}CO (1–0) line maps in the outer Galaxy. We give an overview of the part of the Perseus spiral arm in our outer Galaxy in Section 3. The identification of the Perseus arm structure in position and velocity as well as the regridding of the ^{12}CO data on to a constant linear scale map are outlined in Section 4. This involves the conversion of the spiral arm kinematics and the coordinates from observations into the reference frame of the arm. We present the resulting ^{12}CO data cube at linear scale convolved to the same resolution along the whole arm. Section 5 compares our representation of the Perseus arm in position-velocity with the spiral arm kinematics found in the literature. To study the large scale structure, we analyse the spiral arm kinematics along the arm length, x_{arm}, and the vertical ^{12}CO gas layer structure. We present a summary of our work in Section 6.

2 OBSERVATIONAL DATA

The ^{12}CO J = 1–0 line was mapped in the outer Galaxy in a Galactic longitude range from 55°–194° and a Galactic latitude that is slightly varying along longitude. While the latitude range is restricted to ∼−1°.5 to +2° at a longitude $l = 55°–102°$, the maximum latitude coverage goes from ∼−3°.5 to +5°.5 at $l = 102°–194°$. Observations of the total area are splitted up in two surveys. The FCRAO Outer Galaxy Survey (Heyer et al. 1998) imaged the longitude range between 102°.5 and 141°.5 with a radial velocity range from –154 to 54 km s^{-1}, while the remaining region was mapped subsequently by the Exeter Five College Survey (EXFC; Brunt et al., in preparation). The observed ^{12}CO intensity integrated over all velocities along the line of sight is plotted in Fig. 2. This shows the overall sparse distribution of emission in the outer Galaxy with indication to some
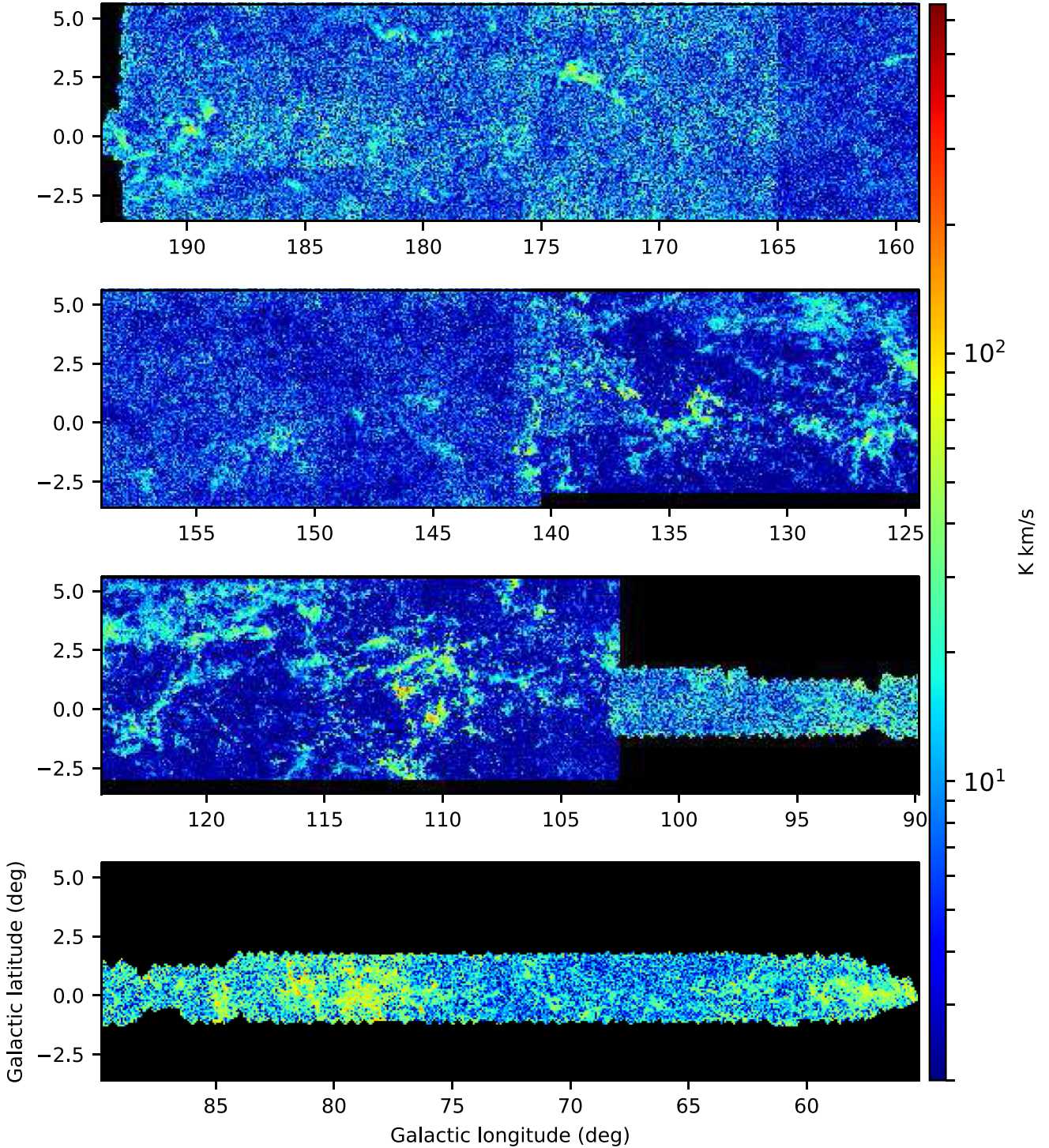
Figure 2. ^{12}CO intensity map of the outer Milky Way from the FCRAO/EXFC observed in the longitude range indicated in Fig. 1 and integrated over all velocities measured along the line of sight.

regions with enhanced ^{12}CO intensity such as those at a Galactic longitude of $\sim$110°, 135°, and 173°. Studies of molecular cloud complexes located in the area observed by the FCRAO/EXFC have been published such as an investigation of their physical conditions (Heyer et al. 2001), in particular their equilibrium state, as well as a principal component analysis within the Perseus and Local spiral arm to characterize turbulence in molecular clouds (Brunt & Heyer 2002) and as a tool to derive their distances (Brunt & Kerton 2002).

The ^{12}CO line was imaged using the FCRAO 14-m telescope. The beamwidth at the frequency of the ^{12}CO (1–0) transition at 115 GHz is 45 arcsec which translates to a size of 2 pc at an average distance of about 9 kpc to the Perseus arm. A short integration time per spectrum
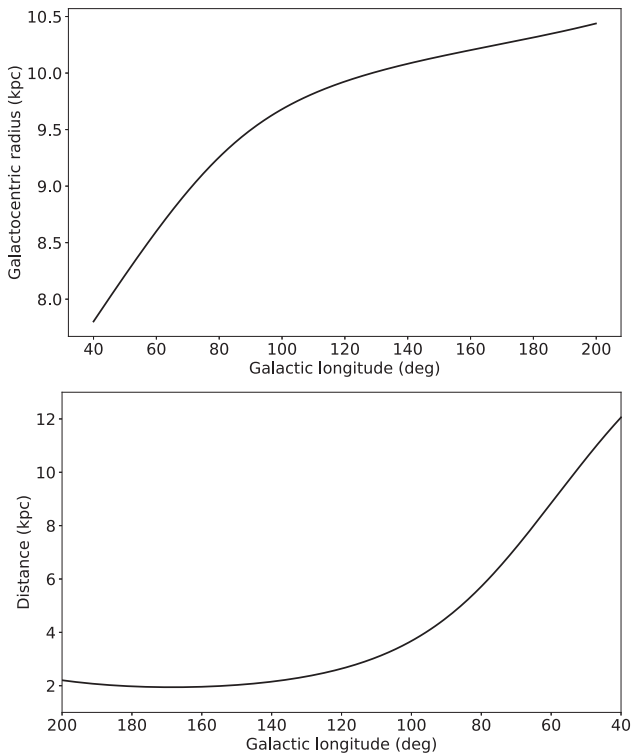
Figure 3. Based on a model for the rotation curve of our Galaxy by Reid et al. (2014), Galactocentric radii are plotted in the upper panel and heliocentric distances in the lower panel as a function of Galactic longitude.

of 10 s was used. ^{12}CO observations were conducted in position-switching mode by the FCRAO survey with a close reference position and the data were sampled every 50 arcsec. The frontend was the FCRAO QUARRY 15 beam array which is used in a frequency range between 86 and 115 GHz. The spectrometers contained 15 autocorrelators with a bandwidth of 80 MHz for each of them. The sampling of the bandwidth was every 313 kHz with a spectral resolution of 0.98 km s^{-1}. An improved array that was present during the Exeter Five College Survey enabled on-the-fly mapping as observing technique and the sampling was per 22.5 arcsec. For that data, we use a velocity resolution regridded to 1 km s^{-1}, although the original data were at a resolution of 0.13 km s^{-1}. A total of 15 x 10^6 spectra in ^{12}CO were obtained. We determined the fluctuation of the noise level after achieving a common velocity resolution of 1 km s^{-1} to be in the range from 3 to 20 mK. This is similar to the temperature fluctuation for the ^{12}CO data at a lower velocity resolution of 0.13 km s^{-1} calculated by Heyer et al. (1998) who give a range between 9 and 15 mK.

3 LOCATION OF THE OUTER PERSEUS SPIRAL ARM IN THE MILKY WAY

An overview of the region presented in this article is given in this section. The Perseus spiral arm is observable in the outer Galaxy between a Galactic longitude of ∼50° and to beyond the anticentre as illustrated by the blue-shaded region in Fig. 1. To set the part of the Perseus spiral arm studied in this article within the context of the Milky Way, the distribution of Galactocentric radii is shown in the top panel of Fig. 3 and heliocentric distances in the bottom panel based on a model for the rotation curve of the Milky Way

(Reid et al. 2014, see Section 4.1.1 for details) against Galactic longitude. The top panel illustrates that we focus on the segment of the Perseus arm that is mainly located at Galactocentric radii > 8 kpc and thus in the outer Milky Way. The Perseus spiral arm is the closest large-scale structure in the Milky Way and covers a span of ∼12 kpc in extent (see Section 4.2.2). The lower panel indicates that a long range in heliocentric distances between 2 and 11 kpc is covered which translates to a variation in spatial resolution along the whole Perseus arm of more than a factor 5. This corresponds to a change in the mass sensitivity of at least a factor 25. Because the aim of this project is to obtain an unbiased comparison of different sections of the spiral arm and a comparison to nearby spiral galaxies, we are mapping the Perseus arm at a common physical resolution from the perspective of an external observer. This involves to first identify the Perseus arm based on its velocities, convert the coordinate system to the Perseus arm reference frame, then smooth the data to a fixed spatial resolution and finally regrid them on to a constant linear scale map described in the following.

4 ANALYSIS AND RESULTS

4.1 Identification of the Perseus arm

4.1.1 Perseus arm kinematic rest frame

We empirically determined the representation of the velocity–longitude structure of the Perseus arm using the logarithmic spiral-arm model derived from Reid et al. (2014) based on maser emission. In particular, the Perseus arm kinematic rest frame is defined based on accurate class II methanol (CH$_3$OH) and water (H$_2$O) maser velocities measured by the BeSSeL survey (Reid et al. 2019). Maser parallaxes provide gold standard distance measurements, even a few are enough to constrain distances with great accuracy. Trigonometric distances which have been deduced from masers measured by the BeSSeL survey therefore allow us to separate the gas emission confined to the Perseus arm from the foreground emission. Eighteen maser parallax distances are currently available along the Perseus arm. Galactic longitude, latitude, LSR velocity, parallax, trigonometric distance, and a reference of those masers are listed in Table 1. We show the longitude–velocity map of ^{12}CO emission integrated over the observed latitude range in Fig. 4 with the maser velocities overlaid in red.

We derived the radial velocity for the longitude range along the Perseus arm using models for the rotation curve from Reid et al. (2014). They measured position, parallax, proper motion, and line-of-sight velocities from Doppler shifts to a sample of ∼100 high-mass star-forming regions within the Milky Way and fitted models of our Galaxy to the 3D position and velocity estimates. Because all motions are measured with respect to the Sun, they modelled the non-circular motion of the Sun which lead to four sets of prior constraints on that. Comparison of the resulting rotation curves and derived parameters such as the distance of the Sun from Galactic Centre, R_0, or the rotation speed of the Milky Way at R_0, let Reid et al. (2014) select model A5 as representative. We adopted their relation between Galactocentric radius and azimuth with the spiral arm parameters resulting from a log-periodic spiral arm fitting. For a given range of azimuths, β, that cover the Perseus arm, we calculated the Galactocentric radius as given in Reid et al. (2014) following

$$r = r_{\text{ref}} \exp(-(\beta - \beta_{\text{ref}}) \tan \psi), \qquad (1)$$

with a reference Galactocentric radius, r_{ref}, of 9.9 kpc fitted at an azimuth, β_{ref}, of 14°2 and a pitch angle, ψ, of 9°4 (cf. Table 2; Perseus

Table 1. Properties of methanol and water masers from Reid et al. (2019).

Source	l (deg)	b (deg)	LSR velocity (km s^{-1})	Parallax (km s^{-1})	Distance (kpc)	Reference
G31.24–00.11	31.24	− 0.11	24.0(±10.0)	0.076(±0.014)	13.16(±2.42)	Wu et al. (2019)
G32.79+0.19	32.79	0.19	16.0(±10.0)	0.103(±0.031)	9.71(±2.92)	Zhang et al. (2019)
G40.42+00.70	40.42	0.70	10.0(±5.0)	0.078(±0.013)	12.82(±2.14)	Hu et al. (in preparation)
G40.62–00.13	40.62	− 0.13	31.0(±3.0)	0.080(±0.021)	12.50(±3.28)	Wu et al. (2019)
G42.03+00.19	42.03	0.19	12.0(±5.0)	0.071(±0.012)	14.08(±2.38)	Hu et al. (in preparation)
W 49N	43.16	00.01	10.0(±5.0)	0.090(±0.007)	11.11(±0.74)	Zhang et al. (2013)
G48.60+00.02	48.60	00.02	18.0(±5.0)	0.093(±0.005)	10.75(±0.58)	Zhang et al. (2013)
G49.26+00.31	49.26	0.31	0.0(±5.0)	0.113(±0.016)	8.85(±1.25)	Zhang et al. (2019)
G49.41+00.32	49.41	0.32	–12.0(±5.0)	0.132(±0.031)	7.58(±1.78)	Zhang et al. (2019)
G70.18+1.74	70.18	1.74	–23.0(±5.0)	0.156(±0.016)	7.35(±0.76)	Sakai et al. (2019)
AFGL 2789	94.60	− 01.79	–43.0(±3.0)	0.221(±0.013)	3.57(±0.38)	Oh et al. (2010), Choi et al. (2014)
G95.29–0.93	95.29	− 0.93	–38.0(±5.0)	0.206(±0.015)	4.88(±0.36)	Hachisuka et al. (2015)
G100.37–3.57	100.37	− 3.57	–37.0(±10.0)	0.289(±0.016)	3.44(±0.12)	Choi et al. (2014)
G108.20+0.58	108.20	0.58	–49.0(±10.0)	0.227(±0.037)	4.37(±0.53)	Choi et al. (2014)
G108.47–2.81	108.47	− 2.81	–54.0(±5.0)	0.309(±0.010)	3.24(±0.10)	Choi et al. (2014)
G108.59+0.49	108.59	0.49	–52.0(±5.0)	0.405(±0.033)	2.51(±0.20)	Choi et al. (2014)
G111.23–1.23	111.23	− 1.23	–53.0(±10.0)	0.300(±0.081)	3.47(±0.53)	Choi et al. (2014)
G111.25–0.76	111.25	− 0.76	–40.0(±3.0)	0.280(±0.015)	3.40(±0.19)	Choi et al. (2014)
NGC 7538	111.54	0.77	–57.0(± 5.0)	0.378(±0.017)	2.65(±0.12)	Moscadelli et al. (2009)
W3(OH)	133.94	1.06	–47.0(±3.0)	0.512(±0.010)	1.95(±0.04)	Xu et al. (2006), Hachisuka et al. (2006)
S Per	134.62	− 2.19	–39.0(± 5.0)	0.413(±0.017)	2.42(±0.10)	Asaki et al. (2010)
G183.72–3.66	183.72	− 3.66	3.0(±5.0)	0.629(±0.012)	1.75(±0.04)	Choi et al. (2014)
IRAS 06061+2151	188.79	1.03	–5.0(±5.0)	0.496(±0.103)	2.02(±0.42)	Niinuma et al. (2011)
S252	188.94	0.88	8.0(±5.0)	0.476(±0.006)	2.10(±0.03)	Reid et al. (2009a), Oh et al. (2010)
G192.16–3.81	192.16	− 3.81	5.0(±5.0)	0.660(±0.040)	1.52(±0.09)	Shiozaki et al. (2011)
S255	192.60	− 00.04	7.0(±5.0)	0.601(±0.039)	1.59(±0.07)	Burns et al. (2017)
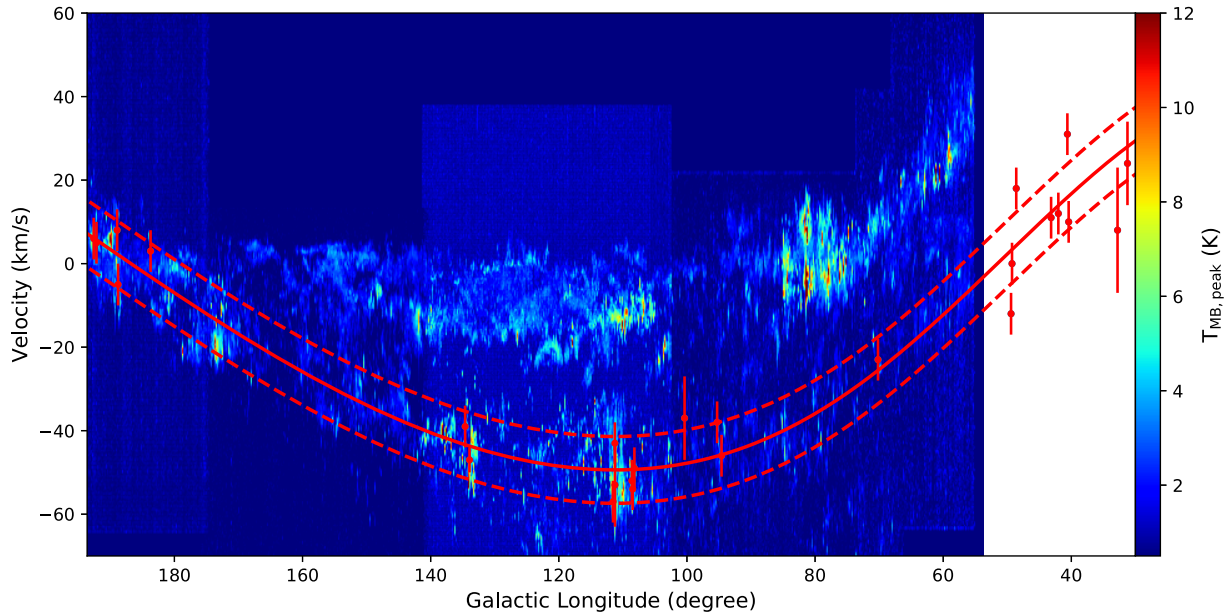
Figure 4. LSR velocities of masers from the BeSSeL survey are plotted against Galactic longitude and overlaid on ^{12}CO (1–0) emission averaged over all Galactic latitudes ($−3°.5 < b < +5°.5$). The red curve shows the kinematic centre of the Perseus arm based on model A5 in Reid et al. (2014). The red dashed curves indicate a velocity window of $±7.8$ km s^{-1} around the arm centre (see Section 4.1.2).

in Reid et al. 2014). Furthermore, we computed the heliocentric distance, d, from

$$r = \sqrt{d^2 \cos^2 b + R_0^2 - 2R_0 d \cos b \cos l}, \qquad (2)$$

where R_0 is the Galactocentric radius of the Sun from model A5, l is Galactic longitude, and b is latitude. The distribution of distances to the Perseus arm based on a log-periodic spiral arm model against longitude is shown in Fig. 3. To derive the line-of-sight velocity to the Perseus arm as reference velocity v_{arm}, we included a radial and

tangential velocity component as suggested by Reid et al. ([2009b](#)), who found that high-mass star-forming regions orbit the Galaxy slower than for circular orbits

$$v_{arm} = R_0 \left(\frac{\Theta_0 + v_t}{r} - \frac{\Theta_0}{R_0} \right) \sin l + v_r \sqrt{1 - \frac{R_0^2 \sin^2 l}{r^2}}, \qquad (3)$$

with the circular rotation speed of the Milky Way, Θ_0, the tangential velocity component, v_t, with respect to Galactic rotation and a radial velocity component, v_r, with regard to the Galactic Centre. We compared the rotation curves using the parameters given in Table 4 in Reid et al. ([2014](#)) resulting from the different priors and found that they all agree within $0.8 \, km \, s^{-1}$. We then choose to use model A5 in the following due to the similarity of the models and because this is considered as representative by Reid et al. ([2014](#)). This model leads to a nearly flat rotation curve with a Galactocentric radius of the Sun of 8.34 kpc and a circular rotation speed of our Galaxy of $240 \, km \, s^{-1}$ at 8.34 kpc.

Spiral arms cause perturbations to the circular orbits along which molecular gas is expected to flow according to the rotation of our Galaxy. Taking spiral induced perturbations into account, we found that the best fit to the line-of-sight velocity of the Perseus arm could be achieved using radial and tangential velocity components that slowly linearly vary with Galactocentric radius. We fitted the LSR velocities of the masers against their longitude according to equation (3), where $v_t = v_{t_0} + \frac{dv}{dr}(r - R_0)$ and $v_r = v_{r_0} + \frac{dv}{dr}(r - R_0)$. Our fit defining the kinematic arm centre as shown as red line in Fig. [4](#) results in $v_{t_0} = -15.33 \, km \, s^{-1}$ with $\frac{dv}{dr} = -1.97 \, km \, s^{-1} \, kpc^{-1}$ and $v_{r_0} = 15.69 \, km \, s^{-1}$ with $\frac{dv}{dr} = -11.25 \, km \, s^{-1} \, kpc^{-1}$. This yields a tangential velocity component with a net perturbation backwards to Galactic rotation. The radial component shows a net perturbation that is changing its direction subject to Galactic location. It is orientated towards the Galactic Centre in the outer Galaxy, at Galactocentric radii larger than 9.4 kpc and $l > \sim 57°$. Approaching the inner Galaxy, at smaller Galactocentric radii and lower longitudes, the net perturbation of the radial component is directed outwards from the Galactic Centre.

4.1.2 Perseus spiral arm width

To transfer to the Perseus arm kinematic rest frame, we extracted for each pixel in Galactic longitude and latitude the ^{12}CO spectrum. This was resampled to a resolution of $1 \, km \, s^{-1}$ and based on equation (3), the reference velocity, v_{arm}, was determined at the corresponding longitude. We subtracted v_{arm} from the ^{12}CO velocity distribution subsequently to shift the velocity axis and to place the kinematic arm centre at $0 \, km \, s^{-1}$. This enabled the extraction of the whole Perseus spiral arm as a coherent feature within a constant velocity window around the kinematic arm centre. To estimate the width of the velocity window, we plot the ^{12}CO line intensity integrated over longitude and latitude on the left-hand axis in Fig. [5](#) as a function of velocity shifted to the Perseus arm kinematic rest frame and fitted the distribution using a Gaussian. This resulted in a standard deviation σ of $6.6 \, km \, s^{-1}$ corresponding to a half width at half-maximum of $7.8 \pm 0.2 \, km \, s^{-1}$ that is used to define the spiral arm width superposed as green shaded area on the Perseus arm velocity distribution illustrated as black line in Fig. [5](#). Our result is in agreement with the standard deviation of the maser velocity distribution of $6.7 \, km \, s^{-1}$. The two peaks at velocities of ~ 15 and $\sim 30 \, km \, s^{-1}$ connected by the grey line belong to the Local and Sagittarius arms.

To confine the Perseus spiral arm and distinguish it from the interarm region, we used the full width at half-maximum (FWHM)
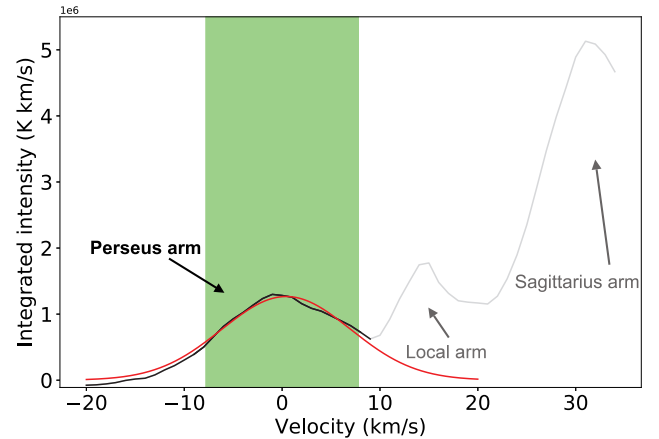
Figure 5. Integrated intensity is plotted on the left-hand axis versus velocities shown as black curve for the Perseus arm and as grey curves for the Local and Sagittarius arms. The velocity distribution of the Perseus spiral arm is marked in green and a Gaussian fit to that is displayed in red.

from the Gaussian fit of $\pm 7.8 \, km \, s^{-1}$ around the kinematic arm centre as spiral arm width marked as dashed lines on the ^{12}CO map in Fig. [4](#). The ^{12}CO data cube in the Perseus arm kinematic rest frame is subsequently limited in velocity to $\pm 7.8 \, km \, s^{-1}$ in order to cover the molecular line emission originating from the spiral arm.

4.2 Perseus spiral arm data cube

4.2.1 Integrated intensity image

We show the ^{12}CO map integrated over the velocity range of $\pm 7.8 \, km \, s^{-1}$ in the Perseus spiral arm kinematic rest frame (see Section 4.1.1) in Fig. [6](#). The irregular boundary at a Galactic Longitude between $\sim 83°$ and $93°$ is caused by limitations of the observations. Extraction of velocities around the arm centre allows us to identify well-known star-forming regions in the spiral arm by the ^{12}CO emission.

NGC 7538 is an H II region ($l = 111°.54, b = 0°.78$) located at a distance of 2.65 kpc (Moscadelli et al. [2009](#)) that harbours three compact radio sources detected at 5 GHz by Martin ([1973](#)). Among those the brightest source is known as IRS 1 that is dominating the far-infrared emission (Wynn-Williams, Becklin & Neugebauer [1974](#); Hackwell, Grasdalen & Gehrz [1982](#)). Furthermore, NGC 7538 is a star-forming region harbouring high-mass main-sequence O-type stars, IRS 5 and IRS 6 being the main ionizing source (Puga et al. [2010](#)).

Another prominent molecular cloud complex is the W3 region consisting of the three H II regions W3, W4, and W5 (Lada et al. [1978](#)). Among those, the brightest molecular cloud is associated with W3 ($l = 133°.5, b = +1°.0$), W4 is a super bubble with an elongated structure around $l = 135°.0, b = -0°.5$), while W5 spreads out the whole complex to $l = 137°.5, b = +1°.5$. These are ideal targets to study the formation and early evolution of high-mass stars. In particular, W3 hosts young high-mass stars that can be distinguished as OB stars, although they have not disrupted their molecular surrounding yet which enables a detailed investigation of a very young star-forming region (Lada et al. [1978](#)). Jose et al. ([2016](#)) focused on the star formation of the molecular cloud AFGL 333 in W3. Estimation of its stellar and cloud mass shows that its density is currently not high enough to form high-mass stars. Furthermore, its
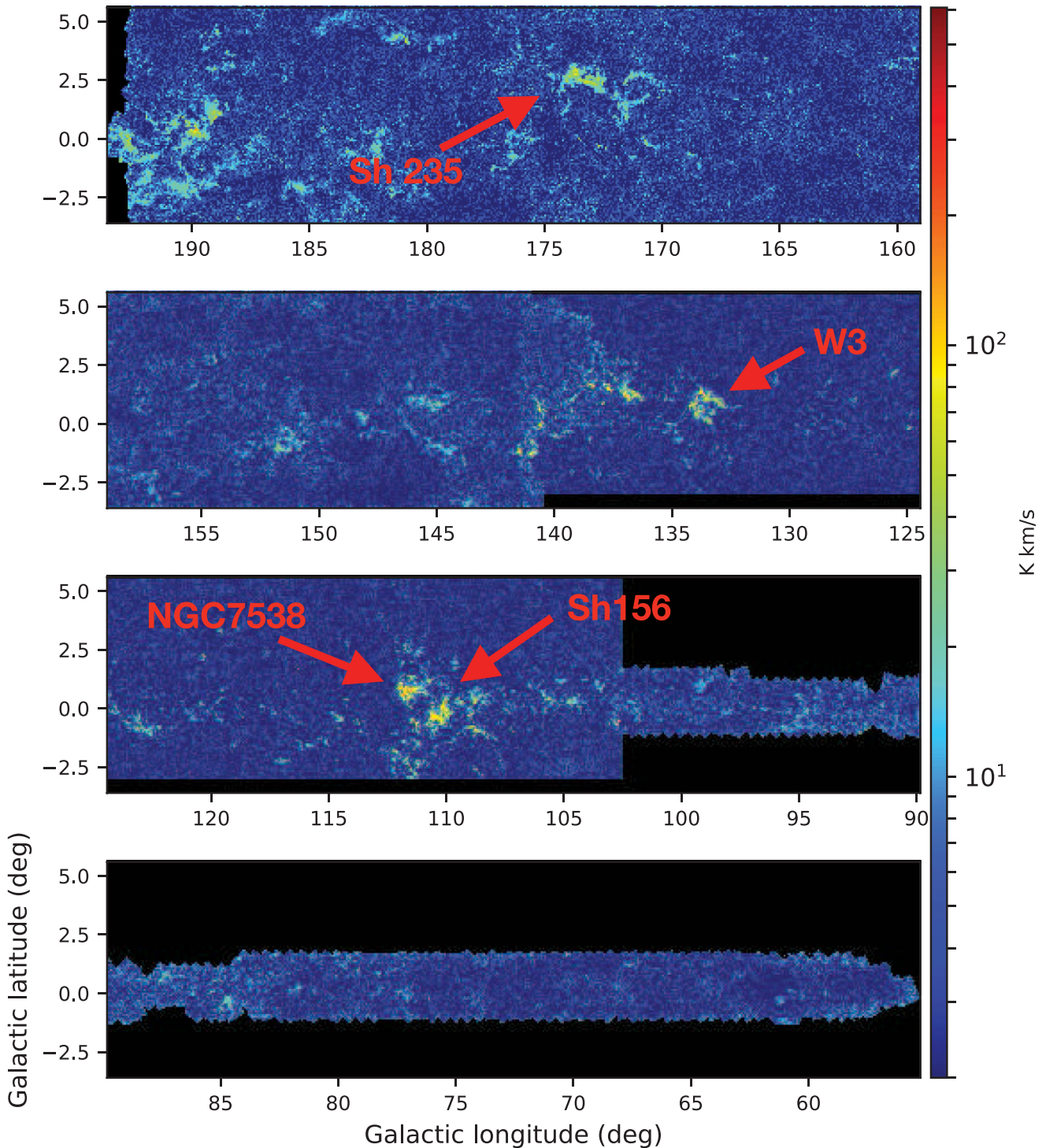
Figure 6. Distribution of ^{12}CO emission towards the Perseus arm in the outer Milky Way integrated over $\pm 7.8\,\mathrm{km\,s^{-1}}$ around the Perseus kinematic arm centre (see Section 4.1.1). Prominent star-forming molecular cloud complexes are labelled in red.

star formation activity is much lower than that of W3 Main which is similar to other massive star-forming regions.

Sharpless 235 at $l \approx 173\overset{\circ}{.}6$, $b \approx +2\overset{\circ}{.}8$ is an H II region with a diameter of $\sim$10 arcmin at the southern boundary of the extended dark cloud Lynds 1518. Sh 235 is associated with a molecular cloud that was observed at optical and millimetre wavelengths by Lafon

et al. (1983). HCO$^+$(1−0) mapping shows two velocity components. One of them at an LSR velocity of −20 km s^{-1} is associated with an optical nebula and the second one at an LSR velocity of −17 km s^{-1} consists of three compact H II regions. Lafon et al. (1983) found similar temperatures, densities, and sizes for the two cloud components, but different star-forming activities. The cloud at

$-20\,\mathrm{km\,s^{-1}}$ harbours two B2–B3 stars, but no compact structures and resembles an H II region at an advanced evolutionary stage. The cloud at $-17\,\mathrm{km\,s^{-1}}$ comprises sources emitting at infrared, Herbig–Haro objects and H_2O maser emission which are all signs of recent and successively occuring star formation.

The nebula Sharpless 156 (IC 1470) at $l = 110°.11$, $b = +0°.05$ is a compact H II region (Israel, Habing & de Jong 1973) associated with a large molecular cloud of 40×25 arcmin^2 identified in H_2CO, OH, and CO by Hoglund & Gordon (1973). It emits intense emission at optical and infrared wavelengths, where it has been investigated in detail by previous studies (Cohen & Barlow 1973; Blair, Peters & vanden Bout 1975; Smutko & Larkin 1999; Zavagno & Ducci 2001; Ghosh & Ojha 2002). According to an analysis in the optical by Heydari-Malayeri, Testor & Lortet (1980), the exciting star causing the observed ionization is of spectral type O7V. They suggest that it formed near the edge of the molecular cloud that has been eroded away so that the star is now located outside the original molecular cloud. This explanation is consistent with the work by Lynds & Oneil (1983) who were able to describe a velocity gradient across the cloud by a model based on this scenario.

4.2.2 Linear scale mapping

After the identification of the Perseus spiral arm and the resampling of the ^{12}CO emission spectrally on to the spiral arm reference frame, we describe the convolution and remapping of the spectral line data cube in the following. As a first step the spatial coordinate system from the observations was converted to the reference frame of the arm (see Appendix A). We transformed Galactic longitude into x_{arm} and Galactic latitude into vertical displacement from the Galactic mid-plane defining the thickness of the Perseus arm. A reference point is defined at a Galactic longitude of 180° corresponding to x_{arm} of 0 pc and rising with decreasing longitude, while a latitude of 0° is assigned to the centre of the Perseus arm's vertical extension and equivalent to the Galactic mid-plane. The total longitude range from $\sim 193°.6$ to $\sim 55°$ is converted to x_{arm} from ~ -0.5 to 11.6 kpc. The maximum latitude extent of $-3°$ to $5°.4$ corresponds to a distance from the mid-plane between -180 and 325 pc. We concentrate to an area of ± 100 pc around the Galactic plane, from where most of the prominent ^{12}CO emission originates.

The next step involves the convolution of the ^{12}CO data at angular resolution to the same spatial resolution along the whole Perseus arm. We first defined a grid for the output data cube of linear scale with a pixel size of 0.5 pc. To smooth the ^{12}CO data at angular resolution, we calculated for each pixel of the output data cube the corresponding position in Galactic coordinates within the observed ^{12}CO data cube according to our coordinate transformation. To convolve the measured ^{12}CO intensity to a chosen fixed spatial resolution of 5 pc, we converted the linear resolution in pc to an angular resolution in degree using the distance at the corresponding longitude taking a correction for the FCRAO telescope beamwidth of 45 arcsec (cf. Section 2) into account. We used a spatially variable kernel convolution algorithm, because the degree of the smoothing depends on the distance from the Perseus arm to the observer: the width of the convolution kernel is larger for nearby molecular gas than for more distant material. To convolve to the chosen fixed linear resolution, θ, we computed a Gaussian, whose FWHM $= \theta$, for every pixel of the ^{12}CO data cube at angular scale within a circle that spans a radius of 4 standard deviations derived from the FWHM of the Gaussian. This also takes a weighting of the pixels according to their distance from the centre of each circle into account. The smoothed

intensity is then written into the corresponding pixel of the output data cube. Repeating this convolution at every pixel of the ^{12}CO data cube along the whole arm results in a Perseus spiral arm cube of constant linear scale that is smoothed to a fixed spatial resolution of 5 pc. Derivation of the noise level of the linear scale data cube at a velocity resolution of $1\,\mathrm{km\,s^{-1}}$ results in a decrease from 60 to 4 mK with increasing Galactic longitude from $\sim 55°$ to 190°, consistent with an increasing width of the convolution kernel.

4.2.3 Common resolution ^{12}CO data cube and data release

A 3D data cube of the Perseus spiral arm with the same spatial resolution along the whole arm was constructed by convolving the angular scale ^{12}CO data cube to a fixed spatial resolution of 5 pc and regridding to a constant linear scale. The Perseus arm length, x_{arm}, the distance from the Galactic mid-plane and velocity difference to the kinematic arm centre as axes of the data cube result from the transformation from angular to linear coordinates. The linear mass surface density map of the ^{12}CO data cube integrated over the velocity range of $\pm 7.8\,\mathrm{km\,s^{-1}}$ in the Perseus arm kinematic rest frame is presented in Fig. 7. To obtain the H_2 gas mass surface density, we converted the integrated ^{12}CO line intensity into the H_2 column density using $X_{\mathrm{CO}} = 2 \times 10^{20}$ cm^{-2} (K km s^{-1})$^{-1}$ (Bolatto, Wolfire & Leroy 2013) and subsequently into the gas mass surface density. This is the first data cube of a spiral arm in our outer Galaxy from the perspective of an external observer that enables future comparison to other galaxies at the same spatial resolution. Fig. 7 illustrates that we cover a segment of a spiral arm in our outer Galaxy with a large span of 12 kpc in extent, which therefore includes wide ranging physical and environmental conditions. In addition, it is the first spiral arm data cube that provides a template for a molecular gas study at fixed spatial resolution. We note that we restrict the distance from the Galactic mid-plane to ± 100 pc as a homogeneously extended area for our analysis despite of the varying latitude coverage of the ^{12}CO data cube.

4.2.4 Scale height distribution

In addition to the molecular gas distribution along x_{arm}, we also investigate the vertical structure of the ^{12}CO gas layer in the Galactic disc. A part of the Perseus spiral arm, within a Galactic longitude between $\sim 84°$ and 102° corresponding to x_{arm} from 3.6 to 5.8 kpc, was not completely homogeneously observed and is covered in a limited latitude range in ^{12}CO. Excluding this region as well as the Galactic anticentre, we integrated along the velocities covered by the Perseus arm of $\pm 7.8\,\mathrm{km\,s^{-1}}$ and along x_{arm} starting at ~ 173 pc, corresponding to $\sim 175°$, to extract ^{12}CO intensities from the linear scale data cube. Integrated intensities are plotted as a function of the distance from the mid-plane in Fig. 8. To convert from integrated intensity to gas mass surface density illustrated on the right-hand axis, we used $X_{\mathrm{CO}} = 2 \times 10^{20}$ cm^{-2} (K km s^{-1})$^{-1}$ (Bolatto et al. 2013) and divided by the arm length as detailed above. A Gaussian function is fitted to the height distribution that gives a scale height as the half-width at half-maximum intensity of $\sim 63 \pm 2$ pc. Our result is in agreement with the scale height found by previous studies. Sanders, Solomon & Scoville (1984) studied molecular clouds in ^{12}CO (1–0) at Galactocentric radii up to 16 kpc and determined a scale height between 60 and 70 pc at galactic radii from 8 to 11 kpc. Modelling of ^{12}CO (1–0) emission at the tangent points by Malhotra (1994) resulted in a scale height of 57 pc of the Galactic disc at the solar radius. A similar, slightly smaller scale height than derived in
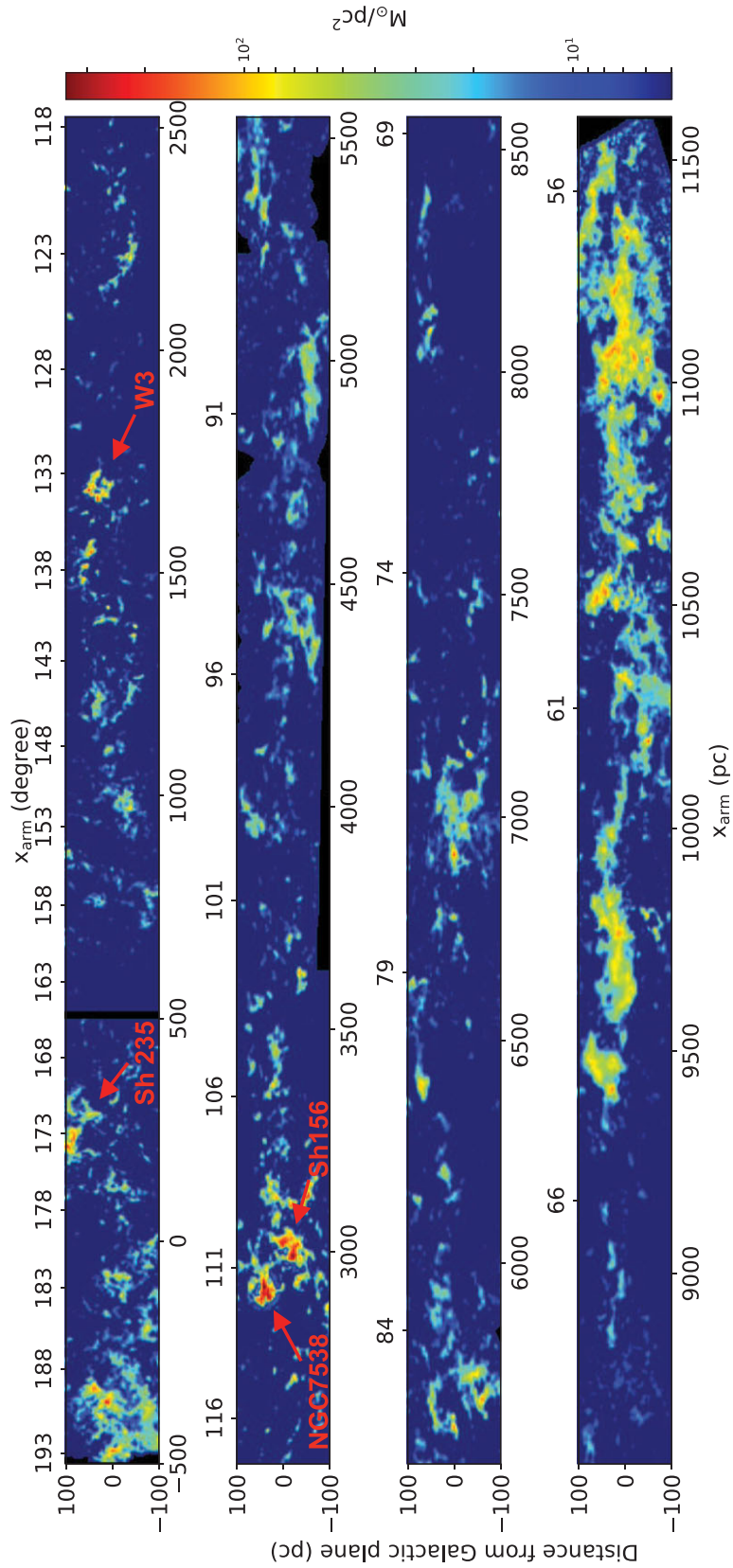
Figure 7. Linear mass surface density image of ^{12}CO emission of the Perseus arm in our outer Galaxy integrated over the velocity range of $\pm 7.8 \, \text{km s}^{-1}$ in the Perseus arm kinematic rest frame (see Section 4.1.1) smoothed to a fixed spatial resolution of 5 pc along the whole spiral arm. The Perseus spiral arm length, x_{arm}, is labelled in deg at the top axis and in pc at the bottom axis.
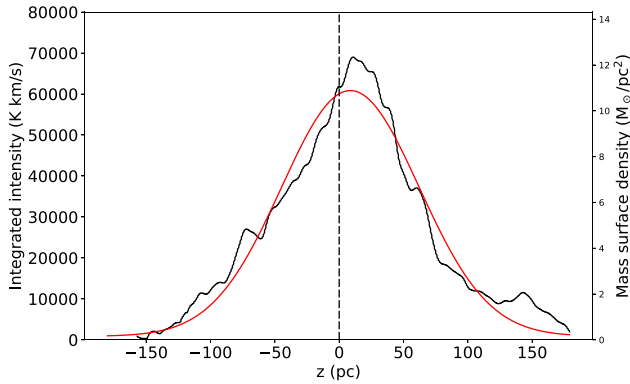
Figure 8. ^{12}CO integrated intensity is displayed on left-hand axis and the mass surface density on the right-hand axis as a function of the distance from the mid-plane. The conversion between the two axes takes the division by the arm length, x_{arm}, into account excluding x_{arm} from 3.6 to 5.8 kpc with limited latitude coverage and starting at $175°$ to exclude the Galactic anticentre. A Gaussian is fitted to the distribution which gives a scale height of $\sim 63 \pm 2$ pc and a distance from the Galactic plane, z, of 8.7 ± 2 pc. The dashed line indicates $z = 0$ pc.

the outer Perseus arm is determined in M51 by Pety et al. (2013). Using their PdBI observations of ^{12}CO (1–0), they obtained ~ 40 pc for the compact component of the disc. Furthermore, Patra (2019) investigated the scale height of a sample of nearby galaxies from the HERA CO-Line Extragalactic Survey (HERACLES; Leroy et al. 2009) observed in CO using the IRAM 30-m telescope. Their study leads to scale heights of the molecular gas discs from 20 to 100 pc in the innermost region of a few kpc which is in agreement with the scale height in the outer Perseus arm. In contrast, the scale height of the atomic gas discs of the HERACLES galaxy sample is found to be twice as high compared to that of the molecular discs.

We determined the mid-plane centroid from the Gaussian fit to the distribution of distances from the Galactic plane in Fig. 8. We found that the peak is located above the Galactic mid-plane at 8.7 ± 1 pc. This is in agreement with the tendency of centroids of the H I layer to be at positive latitudes beyond the solar circle for the northern disc (Henderson, Jackson & Kerr 1982).

We investigated any impact of our analysis excluding x_{arm} between 3.6 and 5.8 kpc with limited latitude coverage. The resulting scale height and displacement from the Galactic mid-plane were, thus, compared to those derived from the integration of the ^{12}CO data cube along the arm thickness of ± 100 pc and the complete arm length. This leads to a scale height of $\sim 59 \pm 4$ pc and a height above the Galactic plane of 6.3 ± 1 pc and therefore indicates that the results from both derivations are consistent.

5 DISCUSSION

5.1 Distance estimates and constraints

For the calibration of the Perseus arm's distance–velocity structure, we used maser parallaxes which involves some uncertainties. The variation of the maser position within the GMC leads to an uncertainty of only 1 per cent in associating masers to GMCs for a typical cloud size of 20 pc at a distance of 2 kpc. The uncertainty is, thus, dominated by a parallax measurement error of 10 per cent at 10 kpc. At a near distance of 2 kpc for clouds not associated with masers, the variation of the cloud position within the spiral arm is prevailing and results in an uncertainty of 20 per cent with a spiral arm width

of ~ 400 pc (Reid et al. 2014). Errors in the association of maser distances to whole GMCs can be neglected, because the error in the parallax distance is usually larger than the radius of the largest GMCs (>50 pc). Due to the distance of GMCs in the Perseus Arm of the order of kpc, the whole GMC can be assumed to be at the same distance.

Although distances to a portion of GMCs in the Perseus arm can be assigned from the maser parallaxes, a number of GMCs remains without exact measure of the LSR velocity. To determine the distances to those GMCs, we assume a single distance as a function of longitude following the rotation curve by Reid et al. (2014). To investigate the deviation of these model distances (see Section 4.1.1) from the trigonometric distances from maser parallaxes and from kinematic distances, we compare the results from the different methods in Fig. 9, where the straight line represents equal distances. The left-hand panel plots the distances that we derived to the Perseus arm based on the model from Reid et al. (2014) (cf. Section 4.1.1) against distances derived from maser parallaxes measured by the BeSSeL survey. The standard deviation of the distribution from equal distances is 1.2 kpc. Our model distances are subsequently compared to kinematic distances calculated from the prescription described in Reid et al. (2009b) in the middle panel. Distances derived from these two methods are in similar agreement as those in the left-hand panel with a standard deviation of 1 kpc. The right-hand panel illustrates the distribution of kinematic distances versus trigonometric distances. The trigonometric distances agree slightly less with the kinematic distances compared to our model distances with a standard deviation of 1.6 kpc. In particular, using the model distances instead of kinematic distances, we avoid an overestimation of distances in the second Galactic quadrant at a distance of 2.5 kpc.
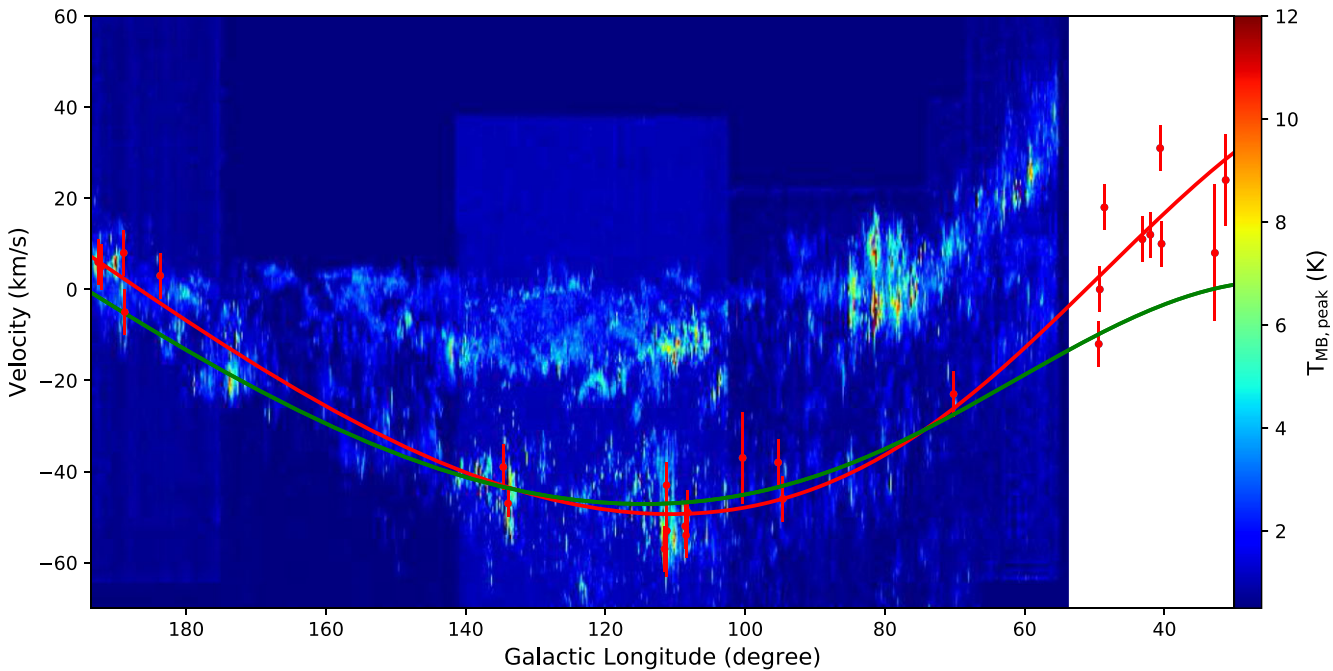
5.2 Longitude–velocity map

As mentioned in Section 4.1.1, the radial and tangential velocity components resulting from our fit to the masers indicate a net motion counter to Galactic rotation as well as a component with respect to the Galactic Centre. Their dependence on the Galactocentric radius suggests that the Perseus arm moves inwards with an increasing radial velocity component towards larger Galactocentric radii, while the arm moves outwards as it approaches the inner Galaxy. The tangential velocity component is rising with decreasing Galactocentric radius. This inward and backward motion is also supported by the analysis of Reid et al. (2014), although they give fixed values for the radial and tangential components. However, these are based on measurements to high-mass star-forming regions within various spiral arms and not derived specifically for the Perseus arm.

Recently, Sakai et al. (2019) studied the kinematics of the Perseus arm using parallaxes and proper motions from the BeSSeL survey. They derived a radial inward motion on average that is counter to Galactic rotation in agreement with our results, but give constant values for the velocity components. We used their result to compute the spiral arm centre velocity according to equation (3) and plot it as red line compared to our fit as green line in Fig. 10. This shows that the two fits are similar over most of the longitude range and start to differ towards smaller longitudes. The deviation likely results from the limitation of the maser positions to a longitude range between $\sim 190°$ and $95°$ fitted by Sakai et al. (2019). The discrepancy of the two curves also supports our variation of the velocity components as a function of Galactocentric radii to be able to fit the velocities of masers in the outer and inner Galaxy down to a longitude of $30°$ simultaneously.
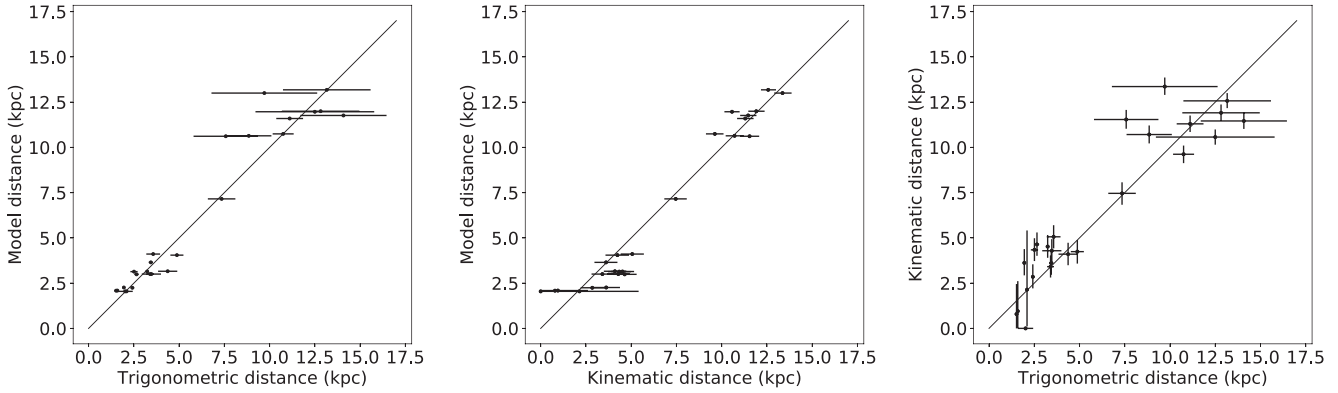
Figure 9. Comparison of the distance computed from the rotation curve of the Milky Way by Reid et al. (2014), the model distance (cf. Section 4.1.1), with the trigonometric distance derived from maser parallaxes in the left-hand panel and with the kinematic distance from Reid et al. (2009b) in the middle panel. The kinematic distance is plotted against trigonometric distance in the right-hand panel. Straight lines in each panel indicate equal distances.


Figure 10. Representation of the longitude–velocity structure of ^{12}CO emission averaged over all Galactic latitudes ($-3°5 < b < +5°5$). Our fit of the Perseus spiral arm based on non-circular motions linearly varying with Galactocentric radius is illustrated as red line, while the fit from Sakai et al. (2019) including fixed velocity perturbations is indicated as green line.

5.3 Perseus arm structure at angular versus linear scale

The distribution of ^{12}CO integrated intensity at angular scale and mass surface density at linear scale along the Perseus arm are compared in Fig. 11. The upper panel shows the longitude–LSR velocity structure of ^{12}CO emission integrated over the observed latitude range. The gas mass surface density map illustrating velocities shifted to the Perseus arm kinematic rest frame against x_{arm} is shown in the bottom panel. To produce the linear mass surface density map, we integrated the ^{12}CO intensity over an area of ± 100 pc around the mid-plane, to which we confine the Perseus spiral arm. Our representation of the Perseus arm structure as derived in Section 4.1.1 at angular scale is indicated as red line in the top panel and corresponds to an arm centre velocity of $0\,\mathrm{km\,s^{-1}}$ illustrated as

red line in the bottom panel. The dashed white lines in the bottom panel mark the width of the Perseus spiral arm and distinguish it from molecular complexes at velocities beyond the Perseus arm velocity window. The mass surface density is scaled to the distance of the Perseus arm and thus refers only to the emission structure within the width of the spiral arm. We illustrate the translation between angular and linear scales of the Perseus arm extent in Fig. 11, where arrows link the Galactic longitude of known molecular cloud complexes to their corresponding position along x_{arm}. The location of Sh 235 at a longitude of $173°6$ is converted to x_{arm} of 0.22 kpc, while W3 at a longitude of $133°5$ can be found at x_{arm} of 1.7 kpc. The two complexes are associated with low mass surface density indicating that only a small amount of mass is contained per pixel at this high longitude end. Furthermore, the location of NGC 7538
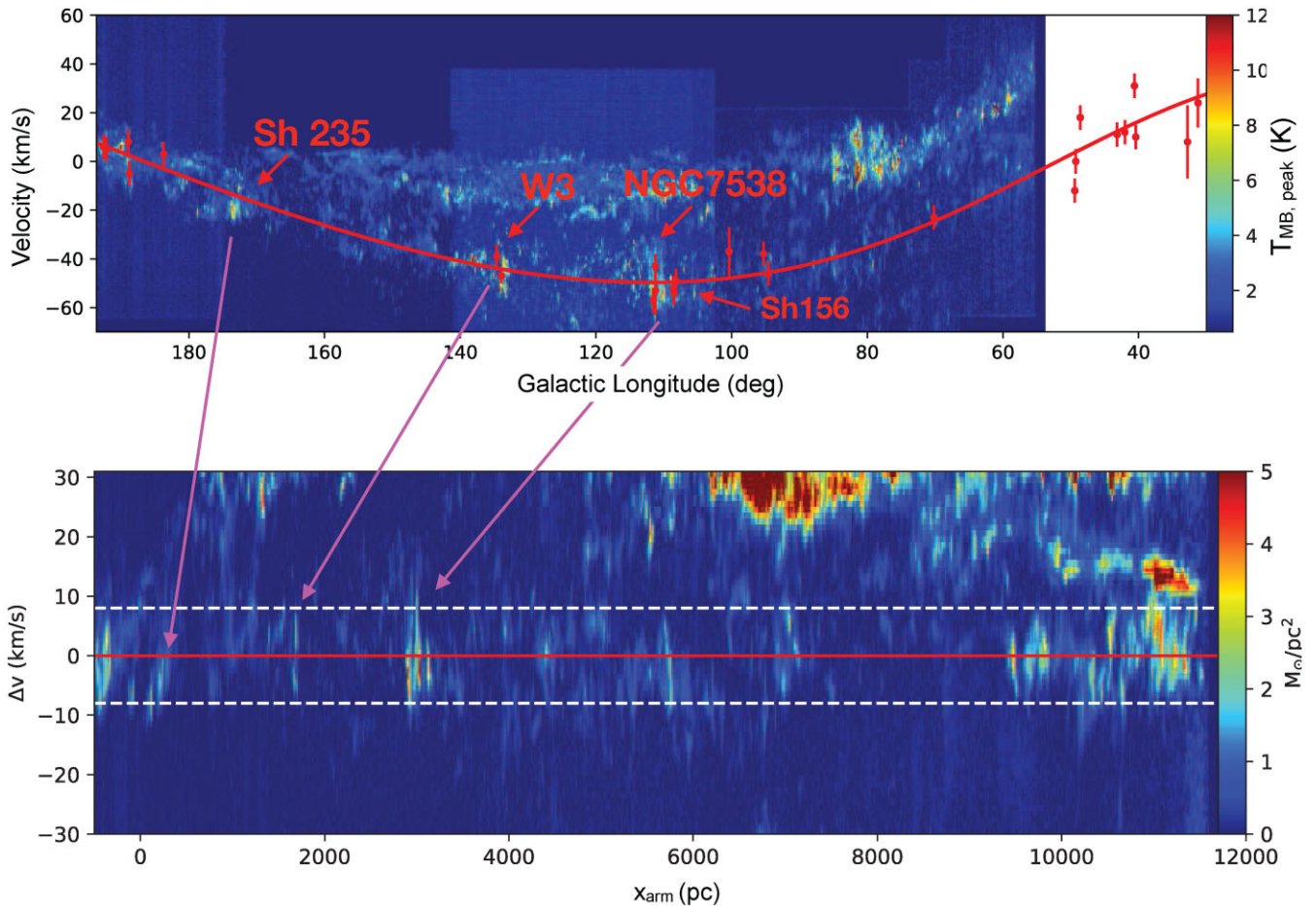
Figure 11. Comparison of the Perseus arm position–velocity diagrams of ^{12}CO emission integrated over the observed latitude range at angular scale in the upper panel and of ^{12}CO mass surface density integrated over a distance of ± 100 pc from the Galactic plane at linear scale in the spiral arm kinematic rest frame in the lower panel. The kinematic arm centre of the Perseus arm is indicated by the red line. The mass surface density illustrated in colour scale is related only to the spiral arm emission inside the velocity window marked by the white dashed lines. Arrows indicate the translation of the location of prominent molecular cloud complexes at Galactic longitude and spiral arm length, x_{arm}.

at a longitude of $111°54$ corresponds to x_{arm} of 2.92 kpc and the position of Sh156 at a longitude of $110°11$ is translated to x_{arm} of 3.03 kpc.

The comparison of these positions in the two reference frames indicates that molecular gas distributed over about half of the longitude range spanned by the Perseus arm is placed within only a quarter of the arm's extent at its intrinsic linear scale resulting from the range of distances to the Perseus arm.

At lower longitudes among several star-forming complexes spread over the region at $l \sim 59°$ are e.g. ultracompact H II regions whose optical spectra, H I 21 cm line in absorption, and H_2CO absorption lines (Fich & Silkey 1990; Watson et al. 2003; Russeil et al. 2011) allowed to derive the far distance to those sites. The mass surface density of those accumulate to the prominent structure of the linear scale data cube at x_{arm} between 10.5 and 11.5 kpc. The conversion from angular to linear scales illustrates that a larger amount of mass is contained per pixel at the low longitude end.

Since the linear mass surface density scale is converted to the distance to the Perseus arm, it is only valid for the structure within the arm window. There are also some molecular cloud complexes at velocities not assigned to the Perseus arm, but present in the velocity range plotted in Fig. 11. Among those is the Cygnus rift at Galactic longitudes between $\sim 79°$ and $82°$ and a LSR velocity

around 0 km s^{-1} (upper panel of Fig. 11). This corresponds to the prominent emission feature at x_{arm} between $\sim$ 6 and 7 kpc and a velocity difference of $\sim$30 km s^{-1} to the kinematic arm centre. The Cygnus rift is an area of diffuse, dark clouds, where hints at the obscuration have first been discovered by star counts by Pyne (1960) in the direction of Cygnus X that is a region of strong and extended radio continuum emission (Piddington & Minnett 1952). Although the Cygnus rift does not make the major contribution to the total gas column density towards Cygnus X, it causes a rise in visual extinction at a distance between 500 and 800 pc obscuring the optical counterparts of radio continuum sources along the line of sight (Schneider et al. 2006). The pathfinder of the ^{12}CO (3–2) survey (Gottschalk et al. 2012) is the first study that distinguished kinematically between the molecular line emission of the rift and other molecular clouds and derived a radial velocity between 0 and 8 km s^{-1}.

At a longitude of $60°$, the Vulpecula Rift is in our local neighbourhood at a LSR velocity of $\sim$20 km s^{-1} (Klaassen et al. 2014). Its position is translated to the velocity difference of $\sim$27 km s^{-1} with respect to the kinematic arm centre at the upper edge of the bottom panel of Fig. 11 at x_{arm} of 11.5 kpc. The Vulpecula Rift is a large molecular cloud complex that is associated with the H II regions Sharpless 86, 87, and 88 (Sharpless 1995) and the open
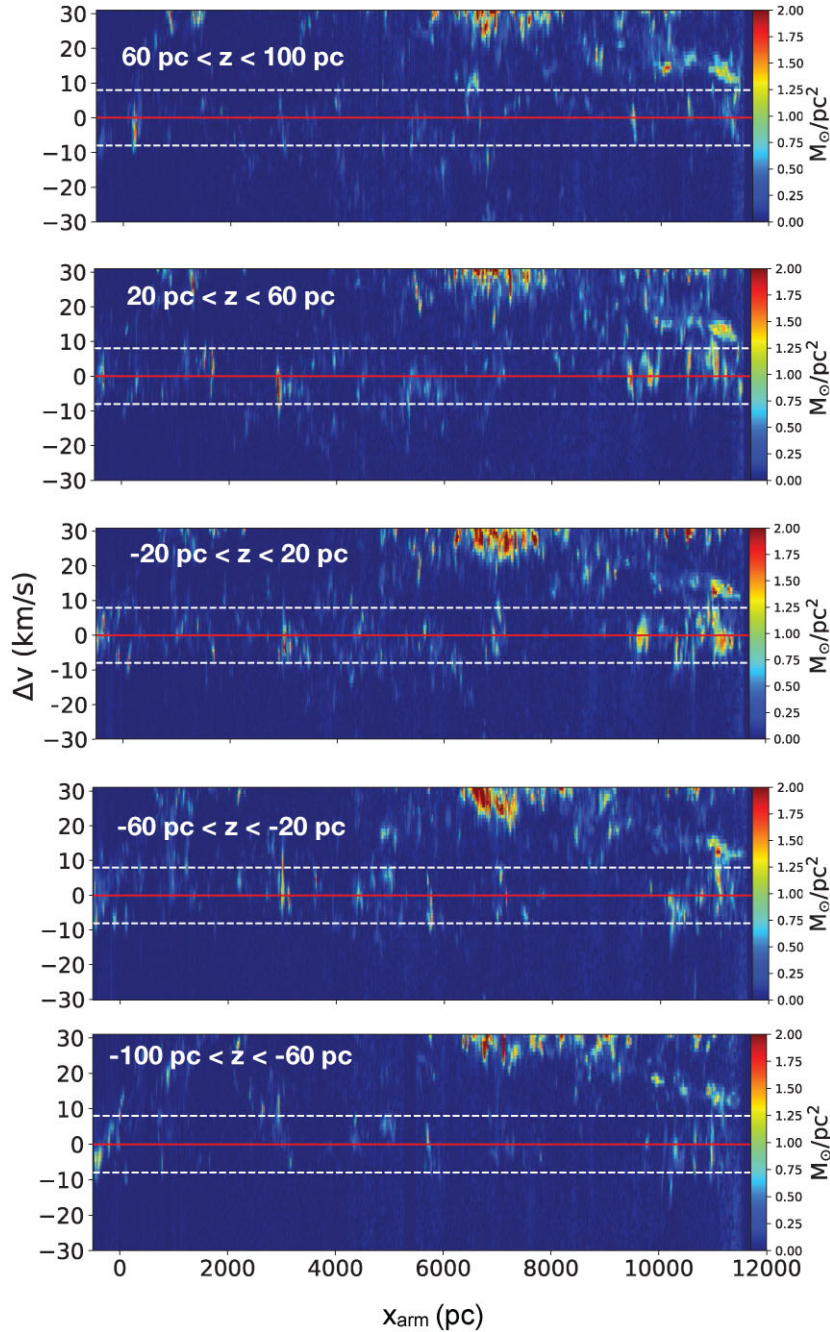
Figure 12. Position - velocity diagrams of ^{12}CO mass surface density integrated over five ranges in distance from the Galactic plane, z. The coverage in distance of each image is labeled.

cluster NGC 6823 as part of the Vul OB 1 association of OB stars (Massey, Johnson & Degioia-Eastwood 1995; Reed 2003). Infrared extinction maps indicate the near distance to the Vulpecula Rift (Russeil et al. 2011) in agreement with the photometric distance of 2.3 kpc to the molecular cloud complex (Massey et al. 1995). There are signs of recent and ongoing star formation in this region such as evolved H II regions, main-sequence OB stars, protostars partially driving very massive and energetic outflows (Beuther et al. 2002) and a still large reservoir of molecular gas and dust. Klaassen et al. (2014) studied the dynamics of a pillar in the Vulpecula Rift ionized by a close high-mass star using CO, ^{13}CO, and $C^{18}O$ lines. They found gas of low temperature at ∼18 K and of low

density, $8 \times 10^3\,\mathrm{cm}^{-3}$, that exhibits a very low velocity dispersion (∼0.5 km s^{-1}) and is likely to move away from the ionizing star.

In addition, some ^{12}CO emission at a longitude of 59° and a LSR velocity of ∼7 km s^{-1} originates from the Sagittarius arm. This is illustrated as the elongated emission structure at a velocity difference of around 15 km s^{-1} and at x_{arm} of 11.5 kpc (bottom panel of Fig. 11) resulting from our conversion to the Perseus arm kinematic frame.

To illustrate the variation of the ^{12}CO mass surface density dependent on the height above/below the Galactic mid-plane, we constructed position velocity diagrams for five bins in height in steps of $\Delta d = 40\,\mathrm{pc}$ in Fig. 12. This shows that most of the large-
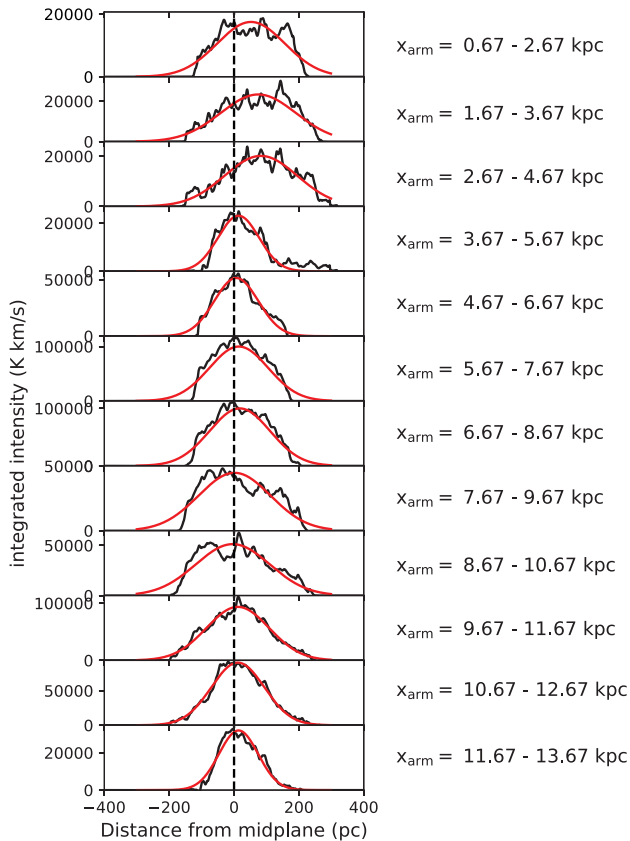
Figure 13. ^{12}CO integrated intensity is plotted against the height above/below Galactic plane for every bin in the Perseus spiral arm length, x_{arm}. The distributions are fitted by a Gaussian. We illustrate $z = 0$ pc by the dashed line.

scale emission features appear predominantly around and above the Galactic mid-plane.

5.4 Variation of arm thickness with Galactic environment

To determine the large-scale variation of the vertical structure of the molecular gas, we divided the ^{12}CO linear scale data cube into bins along x_{arm} and analysed the mass surface density distribution for each bin. The first division was into bins of 2 kpc width along x_{arm} and a second division was added subsequently by shifting each bin by 1 kpc to aim at a homogeneous coverage of the whole Perseus arm including areas of sparse ^{12}CO emission between 7.5 and 9.5 kpc (cf. Fig. 7). The integrated intensity is plotted against distance from the mid-plane for every bin in arm length, x_{arm}, in Fig. 13.

We fitted a Gaussian to the distributions to determine the scale height and the centroid of the molecular gas with the standard error for every x_{arm} bin. To analyse the dependence of the vertical molecular gas structure on the Galactic environment, we converted the mean of each x_{arm} bin into a Galactocentric radius using the relation between the two parameters presented in Fig. A3. Scale heights resulting from the Gaussian fits for each x_{arm} bin against Galactocentric radii show an approximately constant distribution in the upper panel of Fig. 14. Our fit to the data yields a scale height of 76 ± 7 pc on average for the outer Perseus arm illustrated as line in Fig. 14. The dependence of the scale height on the Galactocentric radius has also been studied by previous work. Wouterloot et al. (1990) compiled several H I and CO (1–0) surveys to analyse the large
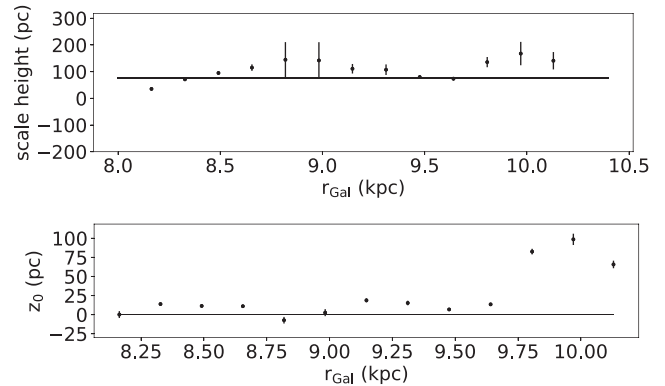
Figure 14. Scale height is shown against Galactocentric radius in the upper panel. A constant scale height fitted to the distribution is indicated by the straight line. The radial distribution of the ^{12}CO layer centroid is presented in the lower panel. The Galactic mid-plane is marked as reference by the straight line.

scale structure of the outer Galaxy. While the H I thickness is larger than that of the molecular gas layer in general, they report only a small increase of both from the solar radius up to 10 kpc in agreement with our result. Clemens, Sanders & Scoville (1988) analysed CO (1–0) maps to derive the distribution of molecular clouds in the first Galactic quadrant. They found no significant change in thickness for the Perseus arm in the outer Galaxy as well. Bronfman et al. (1988) studied CO (1–0) emission of molecular clouds in the Galactic disc within a Galactocentric radius range between 2 and 10 kpc. They derived an approximately constant thickness of the molecular layer with a mean of 70 pc, which is consistent with our result.

Furthermore, the position of the centroid of the ^{12}CO gas layer was determined from the peak of the Gaussian fit to the distributions of the distance from the mid-plane for each x_{arm} bin displayed in Fig. 13. We plot the centroid against the Galactocentric radius which is computed from the mean x_{arm} of each bin in the lower panel of Fig. 14. The distribution is flat between –5 and 20 pc around the Galactic mid-plane labelled by the straight line at $z_0 = 0$ pc up to a Galactocentric radius of ~9.6 kpc. The position of the centroid increases up to 80 pc at Galactocentric radii larger than 9.8 kpc indicating the beginning of the warp of the disc. The centroid of ~100 pc at a Galactocentric radius of 10 kpc is dominated by the star-forming complex Sh 235 (see Section 4.2.1). The radial variation has also been found by previous studies. Clemens et al. (1988) illustrate the offset of the CO gas layer centroid from $b = 0°$ in a face-on image that reveals molecular emission at 50–75 pc above the Galactic plane at 9 kpc. Bronfman et al. (1988) used an axisymmetric model to derive the radial distribution of molecular gas clouds and analysed the deviation of the CO layer from the Galactic plane. They report a displacement of the molecular gas layer of 52 pc at a Galactocentric radius of ~9.75 kpc, where the warp of the disc is beginning and extends beyond the solar circle.

6 CONCLUSIONS

We analysed maps of the ^{12}CO (1–0) line that were observed by the FCRAO survey. The Perseus spiral arm in the outer Galaxy was identified based on its kinematics to produce the first data cube at a common resolution along a whole spiral arm from the perspective of an external observer. Our main results are summarized in this section.

(i) We combined high angular resolution ^{12}CO observations in the outer Galaxy with precise trigonometric distances and line-of-sight velocities from maser parallaxes measured by the BeSSeL survey to separate the gas emission originating from the Perseus spiral arm.

(ii) A logarithmic spiral-arm model (Reid et al. 2014) was used to derive the representation of the velocity–longitude structure of the Perseus arm. The distribution of line-of-sight velocities of masers was investigated to determine an approximation for the width of the spiral arm that is found to be $7.8 \pm 0.2\,\mathrm{km\,s^{-1}}$.

(iii) We changed the coordinate system to the Perseus spiral arm reference frame. The ^{12}CO spectra were shifted to the Perseus arm kinematic arm centre and the data were resampled spectrally on to this reference frame.

(iv) ^{12}CO data were convolved to the same spatial resolution along the whole Perseus arm and regridded on to a constant linear scale map using a spatially variable kernel convolution algorithm. We, thus, produced the first spiral arm data cube at fixed resolution with the length along the Perseus arm, vertical displacement from the Galactic mid-plane and velocity difference to the kinematic arm centre as axes.

(v) The comparison of the longitude–velocity map with the arm length versus velocity difference indicates a large mass per pixel at high longitudes. Molecular gas mass spread over half of the arm's extent at angular coordinates is compressed within only a quarter of the length in the Perseus arm reference frame.

(vi) We derived a scale height of ~63 pc and a centroid of the ^{12}CO gas layer of 8.7 pc from a Gaussian fit to the distribution of distances from the Galactic mid-plane. Our analysis of the variation of these parameters with the Galactic surroundings shows an overall constant distribution of the arm thickness and an approximately similar position of the centroid up to a Galactocentric radius of ~9.6 kpc with an increasing trend at larger radii.

DATA AVAILABILITY

The data underlying this article will be available in the Open Research Exeter (ORE) Repository of the University of Exeter at https://ore.exeter.ac.uk/repository/.

REFERENCES

Anderson L. D., Bania T. M., 2009, ApJ, 690, 706
Asaki Y., Deguchi S., Imai H., Hachisuka K., Miyoshi M., Honma M., 2010, ApJ, 721, 267
Beuther H., Schilke P., Menten K. M., Walmsley C. M., Sridharan T. K., Wyrowski F., 2002, in Crowther P., ed., ASP Conf. Ser. Vol. ASP Conf. Ser. Vol. 267, Hot Star Workshop III: The Earliest Phases of Massive Star Birth. Astron. Soc. Pac., San Francisco, p. 341
Blair G. N., Peters W. L., vanden Bout P. A., 1975, ApJ, 200, L161
Bloemen J. B. G. M. et al., 1984, A&A, 135, 12
Bolatto A. D., Wolfire M., Leroy A. K., 2013, ARA&A, 51, 207
Bronfman L., Cohen R. S., Alvarez H., May J., Thaddeus P., 1988, ApJ, 324, 248
Brunt C. M., Heyer M. H., 2002, ApJ, 566, 289
Brunt C. M., Kerton C. R., 2002, ApJ, 567, L41
Burns R. A. et al., 2017, MNRAS, 467, 2367
Busfield A. L., Purcell C. R., Hoare M. G., Lumsden S. L., Moore T. J. T., Oudmaijer R. D., 2006, MNRAS, 366, 1096
Chen B., et al. 2016, AJ, 152, 45
Choi Y. K., Hachisuka K., Reid M. J., Xu Y., Brunthaler A., Menten K. M., Dame T. M., 2014, ApJ, 790, 99
Clemens D. P., Sanders D. B., Scoville N. Z., 1988, ApJ, 327, 139
Cohen M., Barlow M. J., 1973, ApJ, 185, L37
Colombo D. et al., 2014, ApJ, 784, 3
Colombo D. et al., 2019, MNRAS, 483, 4291
Dame T. M., Hartmann D., Thaddeus P., 2001, ApJ, 547, 792
Donovan Meyer J. et al., 2013, ApJ, 772, 107
Fich M., Silkey M., 1990, BAAS, 22, 1304
Freeman P., Rosolowsky E., Kruijssen J. M. D., Bastian N., Adamo A., 2017, MNRAS, 468, 1769
García P., Bronfman L., Nyman L.-Å., Dame T. M., Luna A., 2014, ApJS, 212, 2
Ghosh S. K., Ojha D. K., 2002, A&A, 388, 326
Giannetti A. et al., 2017, A&A, 606, L12
Gottschalk M., Kothes R., Matthews H. E., Land ecker T. L., Dent W. R. F., 2012, A&A, 541, A79
Gratier P. et al., 2010, A&A, 522, A3
Gratier P. et al., 2012, A&A, 542, A108
Hachisuka K. et al., 2006, ApJ, 645, 337
Hachisuka K., Choi Y. K., Reid M. J., Brunthaler A., Menten K. M., Sanna A., Dame T. M., 2015, ApJ, 800, 2
Hackwell J. A., Grasdalen G. L., Gehrz R. D., 1982, ApJ, 252, 250
Helfer T. T., Thornley M. D., Regan M. W., Wong T., Sheth K., Vogel S. N., Blitz L., Bock D. C.-J., 2003, ApJS, 145, 259
Henderson A. P., Jackson P. D., Kerr F. J., 1982, ApJ, 263, 116
Heydari-Malayeri M., Testor G., Lortet M. C., 1980, A&A, 84, 154
Heyer M. H., Brunt C., Snell R. L., Howe J. E., Schloerb F. P., Carpenter J. M., 1998, ApJS, 115, 241
Heyer M. H., Carpenter J. M., Snell R. L., 2001, ApJ, 551, 852
Heyer M., Dame T. M., 2015, ARA&A, 53, 583
Hoglund B., Gordon M. A., 1973, ApJ, 182, 45
Hughes A. et al., 2013, ApJ, 779, 46
Israel F. P., Habing H. J., de Jong T., 1973, A&A, 27, 143
Jose J., Kim J. S., Herczeg G. J., Samal M. R., Bieging J. H., Meyer M. R., Sherry W. H., 2016, ApJ, 822, 49
Klaassen P. D., Mottram J. C., Dale J. E., Juhasz A., 2014, MNRAS, 441, 656
Lada C. J., Elmegreen B. G., Cong H. I., Thaddeus P., 1978, ApJ, 226, L39
Lafon G., Deharveng L., Baudry A., de La Noë J., 1983, A&A, 124, 1
Leroy A. K. et al., 2009, AJ, 137, 4670
Leroy A. K. et al., 2015, ApJ, 801, 25
Lynds B. T., Oneil E. J. J., 1983, ApJ, 265, 803
Malhotra S., 1994, ApJ, 433, 687
Martin A. H. M., 1973, MNRAS, 163, 141
Massey P., Johnson K. E., Degioia-Eastwood K., 1995, ApJ, 454, 151
Meidt S. E. et al., 2013, ApJ, 779, 45
Miville-Deschênes M.-A., Murray N., Lee E. J., 2017, ApJ, 834, 57
Moscadelli L., Reid M. J., Menten K. M., Brunthaler A., Zheng X. W., Xu Y., 2009, ApJ, 693, 406
Muraoka K. et al., 2016, PASJ, 68, 18
Niinuma K. et al., 2011, PASJ, 63, 9
Oh C. S., Kobayashi H., Honma M., Hirota T., Sato K., Ueno Y., 2010, PASJ, 62, 101
Pan H.-A., Kuno N., 2017, ApJ, 839, 133
Patra N. N., 2019, MNRAS, 484, 81
Pettitt A. R., Ragan S. E., Smith M. C., 2020, MNRAS, 491, 2162
Pety J. et al., 2013, ApJ, 779, 43
Piddington J. H., Minnett H. C., 1952, Aust. J. Sci. Res. A, 5, 17

Puga E. et al., 2010, A&A, 517, A2
Pyne A. C., 1960, AJ, 65, 154
Reed B. C., 2003, AJ, 125, 2531
Reid M. J. et al., 2009b, ApJ, 700, 137
Reid M. J. et al., 2014, ApJ, 783, 130
Reid M. J. et al., 2019, ApJ, 885, 131
Reid M. J., Dame T. M., Menten K. M., Brunthaler A., 2016, ApJ, 823, 77
Reid M. J., Menten K. M., Brunthaler A., Zheng X. W., Moscadelli L., Xu
    Y., 2009a, ApJ, 693, 397
Rice T. S., Goodman A. A., Bergin E. A., Beaumont C., Dame T. M., 2016,
    ApJ, 822, 52
Roman-Duval J., Jackson J. M., Heyer M., Johnson A., Rathborne J., Shah
    R., Simon R., 2009, ApJ, 699, 1153
Roman-Duval J., Jackson J. M., Heyer M., Rathborne J., Simon R., 2010,
    ApJ, 723, 492
Rosolowsky E., Blitz L., 2005, ApJ, 623, 826
Rudolph A. L., Simpson J. P., Haas M. R., Erickson E. F., Fich M., 1997,
    ApJ, 489, 94
Russeil D. et al., 2011, A&A, 526, A151
Sakai N., Reid M. J., Menten K. M., Brunthaler A., Dame T. M., 2019, ApJ,
    876, 30
Sanders D. B., Solomon P. M., Scoville N. Z., 1984, ApJ, 276, 182
Schinnerer E. et al., 2013, ApJ, 779, 42
Schneider N., Bontemps S., Simon R., Jakob H., Motte F., Miller M., Kramer
    C., Stutzki J., 2006, A&A, 458, 855
Sewilo M., Watson C., Araya E., Churchwell E., Hofner P., Kurtz S., 2004,
    ApJS, 154, 553
Sharpless S., 1995, VizieR Online Data Catalog, p. VII/20
Shiozaki S., Imai H., Tafoya D., Omodaka T., Hirota T., Honma M., Matsui
    M., Ueno Y., 2011, PASJ, 63, 1219
Smutko M. F., Larkin J. E., 1999, AJ, 117, 2448
Solomon P. M., Rivolo A. R., 1989, ApJ, 339, 919
Tosaki T. et al., 2017, PASJ, 69, 18
Vallée J. P., 2014, ApJS, 215, 1
Watson C., Araya E., Sewilo M., Churchwell E., Hofner P., Kurtz S., 2003,
    ApJ, 587, 714
Wienen M. et al., 2015, A&A, 579, A91
Wouterloot J. G. A., Brand J., Burton W. B., Kwee K. K., 1990, A&A, 230,
    21
Wu Y. W. et al., 2019, ApJ, 874, 94
Wynn-Williams C. G., Becklin E. E., Neugebauer G., 1974, ApJ, 187, 473
Xu Y., Reid M. J., Zheng X. W., Menten K. M., 2006, Science, 311, 54
Zavagno A., Ducci V., 2001, A&A, 371, 312
Zhang B. et al., 2019, AJ, 157, 200
Zhang B., Reid M. J., Menten K. M., Zheng X. W., Brunthaler A., Dame T.
    M., Xu Y., 2013, ApJ, 775, 79

## APPENDIX A: CONVERSION OF THE COORDINATE SYSTEM

We provide details about the transformation from the angular coordinate system to the linear scale Perseus arm reference frame in this section. Galactic longitude is converted to x_{arm}. We set a Galactic longitude of $180°$ as reference point corresponding to x_{arm} of $0\,pc$, which is increasing with lowering longitude. According to Reid et al. (2016), the shape and alignment of spiral arm tracks resemble those of logarithmic spiral arms. Our calculation of x_{arm} is visualized in Fig. A1. To follow the length along the arm track, we split the Perseus arm into tiny segments, calculate their extent, and sum those up subsequently. The length of each segment is calculated by

$$\Delta x = \sqrt{d_1^2 + d_2^2 - 2\,d_1\,d_2\,\cos(\ell_1 - \ell_2)}, \qquad (A1)$$
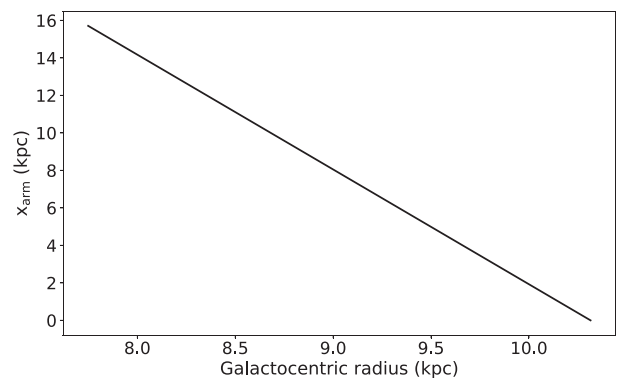
where ℓ_1 and ℓ_2 are Galactic longitudes of two endpoints of an arm segment Δx and d_1 and d_2 the distance from the Sun to those
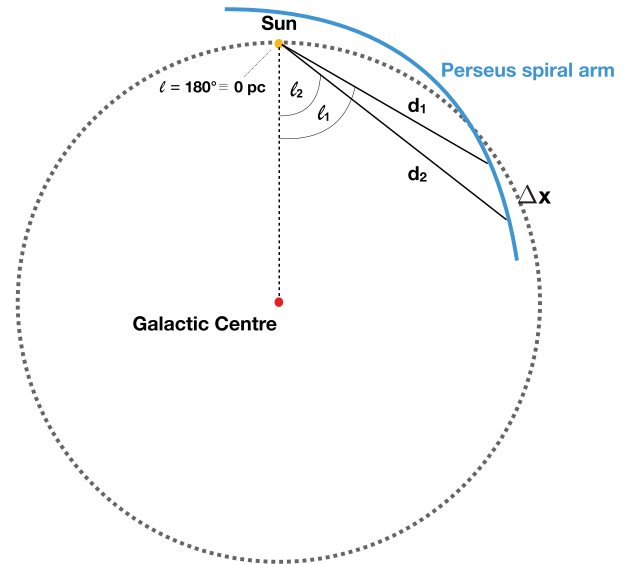
Figure A1. Schematic description of the computation of Perseus spiral arm length, x_{arm}.
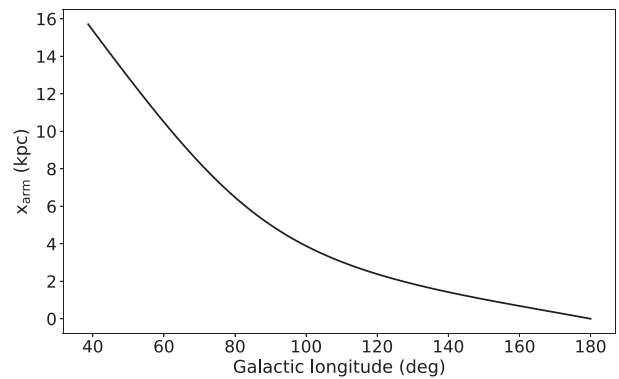
Figure A2. Relation between Galactic longitude and length of the outer Perseus spiral arm, x_{arm}.

Figure A3. Correlation plot between the Galactocentric radius and the Perseus arm length, x_{arm}.

endpoints. Adding the lengths of all segments up along the spiral arm track from the Galactic anticentre until a Galactic longitude of 31° results in a total extent of 12 kpc of the Perseus arm in the outer Galaxy. For the part of the spiral arm between the anticentre and a Galactic longitude of 193°.6, we computed a length of 500 pc. This extension is assigned to negative values in the linear data cube (cf. Fig. 7) indicating the opposite direction compared to the rest of the spiral arm cube. We plot x_{arm} against Galactic longitude in Fig. A2. To illustrate the location of the Perseus arm with respect to the Galactic environment, we show the distribution of x_{arm} against Galactocentric radius derived from equation (1) in Fig. A3.

The thickness of the Perseus spiral arm is derived from Galactic latitude. The centre of the vertical ^{12}CO gas layer structure is defined to be at a Galactic latitude of 0° and thus in the Galactic mid-plane. We converted from angular to linear scale using the distance to the Perseus arm which is calculated for each longitude as given in equation (2). This results into a distance of 325 pc above the Galactic plane for the maximum positive latitude extension of 5°.4 and into a distance of 180 pc below the plane for the maximum coverage towards negative latitudes of –3°. For our analysis of the Perseus spiral arm, we focus on the region of ±100 pc around the mid-plane, where the bulk of the ^{12}CO emission comes from.

This paper has been typeset from a TEX/LATEX file prepared by the author.